ELSEVIER

Organic Electronics 3 (2002) 129–141

Organic Electronics

www.elsevier.com/locate/orgel

The internal electric field distribution in bilayer organic light emitting diodes

Simon J. Martin [a], Geraldine L.B. Verschoor [b], Matthew A. Webster [a], Alison B. Walker [a,*]

[a] *Department of Physics, University of Bath, Bath BA2 7AY, UK*

[b] *Sharp Laboratories of Europe, Edmund Halley Rd, Oxford Science Park, Oxford OX4 4GA, UK*

Received 20 February 2002; received in revised form 13 May 2002; accepted 15 July 2002

Abstract

The internal electric field distribution in a bilayer 4,4′-bis[*N*-(1-napthyl)-*N*-phenylamino]-biphenyl/tris-(8-hydroxyquinoline) aluminium organic light emitting diode has been investigated experimentally using electroabsorption spectroscopy. The experimental results have been compared to those obtained from a drift–diffusion device simulation, further validating the model and highlighting the potential worth of such modelling. With the aid of the simulation, the electric field distribution can be explained in terms of charge carrier accumulation at the interface between the two organic layers, due to the HOMO and LUMO band offsets, and charge injection into the device, demonstrating the influence of contact materials on device behaviour.

PACS: 73.61.Ph

Keywords: OLED; Electroabsorption spectroscopy; Bilayer; Device simulation

1. Introduction

Since the fabrication of the first successful organic light emitting diodes (OLEDs) by Tang and VanSlyke [1,2], good progress has been made in improving these devices for use in practical applications, notably including the use of conjugated polymers [3]. However, there is still much debate over the nature of charge injection, transport and distribution in OLEDs, both in single and multilayer devices.

Much of the work done to characterise these devices has focused on their current–voltage (J–V) and current–luminance characteristics. However, the charge carrier distributions in these devices relate directly to the internal electric field via Poisson's equation. The investigation into the internal electric fields by electroabsorption (EA) spectroscopy may help explain the charge distribution in bilayer OLEDs [4–6], and hence enable the design of more efficient devices. Charge accumulation within a device alters the electric field within the device, which ultimately affects charge injection and transport. Recently, the internal potential distribution in a bilayer OLED has been measured by inserting a third electrode into the bulk [7], but this method has a spatial resolution of

* Corresponding author. Tel.: +1-225-32-3322; fax: +1-225-82-6110.

E-mail address: a.b.walker@bath.ac.uk (A.B. Walker).

1566-1199/02/$ - see front matter
PII: S1566-1199(02)00050-2

about 100 nm, greater than the typical thickness of a device layer.

EA spectroscopy uses an electric field to modulate the transmission of light through an OLED by perturbing the energy levels of the organic layers [8]. Applying both an ac bias of frequency Ω and a dc bias to the device causes the formation of a dc internal electric field within the device. This field is due to the external dc bias plus the built-in potential (V_{bi}) of the device. The ac bias does not contribute to the internal field, provided that Ω is large enough such that the charge distribution is unaffected ($\Omega \sim$ kHz).

In this paper, we compare the electric field distributions measured in bilayer 4,4′-bis[*N*-(1-napthyl)-*N*-phenylamino]-biphenyl (NPB)/tris-(8-hydroxyquinoline) aluminium (Alq) devices by EA spectroscopy with those obtained from a device simulation. The devices studied were fabricated from layers of 40 nm thick Alq and NPB, with an ITO anode and either an Al or Al:Li cathode. Fig. 1 shows a schematic energy level diagram for an ITO/NPB/Alq/Al device [9,10]. Average electric fields in each of the organic layers (NPB and Alq) have been calculated from the EA data as a function of applied bias for both the ITO/NPB/Alq/Al and ITO/NPB/Alq/Al:Li devices.

The devices were simulated using a one-dimensional time-independent drift–diffusion model, which has also been used to investigate *J–V* characteristics of OLEDs [11]. This model is similar to those presented else where in the literature (e.g. [12–14]). The simulation produces electric field profiles for the devices, from which average field values can easily be obtained, and carrier density profiles to aid the explanation of the field distributions. The model was also used to simulate the electric field distribution in an ITO/NPB/Alq/Mg:Ag device, which had been investigated experimentally using EA spectroscopy by Rohlfing et al. [4,15]. Our model reproduces closely the data in Rohlfing et al. [4] for the average field in the NPB layer. Our model predictions for the average field in the Alq layer track the measured data in [4] but the modelled fields are much greater.

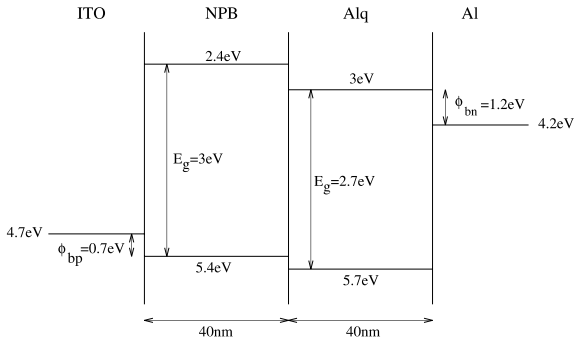

Fig. 1. Schematic band diagram of ITO/NPB/Alq/Al:Li device.

There have been other theoretical calculations of the electric field distributions in bilayer OLEDs [16–18], but this is the first time to the authors' knowledge that direct comparisons have been made between theory and experiment. In [17] the same contacts are used as for the device of Rohlfing et al. [4] with TPD replacing NPB, but this material is very similar to NPB. At low biases, up to about 4 V, the predictions for the field in the Alq layer from our model agree well with those of Ruhstaller et al. [17]. At higher biases however, the average field in the Alq layer increases with bias contrary to our predictions and the results of Rohlfing et al. [4]. Furthermore, Ruhstaller et al. [17] predict very little variation in the average field in the NPB layer with bias, again in disagreement with our results and those of Rohlfing et al. [4].

2. Experimental method

2.1. EA technique

The fundamental EA response (i.e. under an applied ac bias at frequency Ω) of a particular organic layer at a particular wavelength of light is proportional to the imaginary part of the third order nonlinear susceptibility, $\Im\chi^{(3)}(h\nu)$, and the square of the total electric field,

$$\frac{\Delta I}{I}(h\nu) \propto \Im\chi^{(3)}(h\nu)E_{tot}^2, \tag{1}$$

where $\Delta I/I$ is the change in transmitted light intensity (the measured EA signal), $h\nu$ is the photon energy, and E_{tot} is the total electric field, consisting of the interfacial field E_i, an applied dc component

of magnitude E_{dc}, and an applied ac component at frequency Ω of magnitude E_{ac} (thus $E_{tot} = E_i + E_{dc} + E_{ac}\cos(\Omega t)$). The dc component consists of two contributions: one from the built-in field, and one from the external applied field. E_i is observed in low molar mass materials and is likely to originate from interface states, such as charge transfer induced dipoles between the metal/organic interface, which shift the molecular energy levels of the organic material relative to those of the metal [6].

Hence the EA response is given by

$$\frac{\Delta I}{I}(h\nu) \propto \Im\chi^{(3)}(h\nu)[(E_i + E_{dc})^2 + \{2E_{ac}(E_i + E_{dc})\}\cos(\Omega t) + E_{ac}^2(1 + \cos(2\Omega t))/2]. \quad (2)$$

If $E_i + E_{dc} \neq 0$, the EA response is modulated at both the fundamental (Ω) and second harmonic (2Ω) frequency of the applied ac bias. The response at the fundamental frequency is

$$\frac{\Delta I}{I}(h\nu; \Omega) \propto \Im\chi^{(3)}(h\nu)\{2E_{ac}(E_i + E_{dc})\}\cos(\Omega t), \quad (3)$$

and the response at the second harmonic is given by

$$\frac{\Delta I}{I}(h\nu; 2\Omega) \propto \Im\chi^{(3)}(h\nu)(E_{ac}^2/2)\cos(2\Omega t). \quad (4)$$

The magnitude of the internal electric field is determined by measuring the EA signal at both the fundamental (Ω) and second harmonic frequency (2Ω) of the ac bias, and comparing the signal amplitudes to reference spectra obtained under known biases. Different materials give different EA responses at different wavelengths, so by performing EA measurements on single layer devices of the constituent materials of the bilayer device, the fields in each layer can be identified from the bilayer EA signal. The internal electric field obtained from EA measurements is an average value of the electric field within a particular layer, although this technique has been extended to probe the electric field distribution in a device [4,5].

2.2. Experimental details

The LEDs were fabricated on 20Ω/square ITO on a glass substrate. The ITO anode was patterned using conventional photolithography. Before organic deposition, the ITO was subjected to a wet cleaning procedure including sonication in a solutions of detergent and NaOH and rinsing in deionised water and propan-2-ol. The LEDs consisted of 40 nm NPB as the hole transport layer and 40 nm Alq as the electron transport and emitting layer. The NPB and Alq were supplied by Kodak and were EL grade. The organic layers and metal cathode were deposited by thermal sublimation in a Pfeiffer PLS 500 system. The sublimation rate for the organic materials was between 0.2 and 0.4 nm/s (measured using an oscillating crystal monitor) and the pressure during sublimation was below 7×10^{-7} mbar. The cathode was defined by a shadow mask and comprised of either Al or an Al:Li alloy. The alloy was made by co-evaporating the Al and Li, the Al rate being approximately 10 times as large as the Li rate [19]. The cathode thickness was 200 nm and defined a device area of 4 mm^2. After fabrication the OLEDs were immediately transferred into a dry nitrogen glove box where they were encapsulated using a glass cover and an epoxy seal.

The EA measurements were carried out in the reflection mode. This enabled thinner layers to be studied than if the measurement was made in transmission mode. Hence more realistic devices could be studied than in the study by Rohlfing et al. [4]. Broadband light from a 150 W Xenon lamp was monochromated by a Digikrom 240 monochromator, and focused onto the LED at $\approx$45° through the ITO electrode. The light was specularly reflected off the back metal electrode and focused on to a UV enhanced photodiode. The applied voltage consists of a dc voltage with a superimposed ac component of 5 kHz. The photodetector output was amplified by an EG&G 5182 preamplifier, which separates out the dc and ac components of the signal. The dc component was measured by a Keithley 2000 multimeter, and the ac component was measured by a Stanford SR830 lock-in. Above the turn on voltage, an optical

bandpass filter was used to block the emission of light from the LED.

The barrier height to electron injection into the Alq LUMO with the two different cathodes was compared using internal photoemission [20]. Monochromatic light of energy hv which was lower than the band gap of the organic material was chopped with a chopper wheel and focused onto the device from the ITO side. Carriers at the Fermi level of the cathode are excited over the energy barrier between the cathode and the LUMO of the organic material. The resulting photocurrent was detected with a lock in amplifier. The relationship between the photocurrent and the energy of the incident light is given by Fowler's theory [21] and is $I_{\mathrm{IPE}} \sim (hv - \Phi_{\mathrm{B}})^2$ where I_{IPE} is the photocurrent and Φ_{B} is the energy barrier. Therefore a graph of the square root of the photocurrent versus photon energy gives a straight line with an intercept on the energy axis of Φ_{B}.

Fig. 2 shows this for a ITO/Alq(130 nm)/Al device and a ITO/Alq(130 nm)/Al:Li device. For the device with the Al cathode, the electron injection barrier, Φ_{B} was measured to be 1.1 ± 0.2 eV. This is in good agreement with other reported values of this barrier [20]. For the device with an Al:Li cathode, Φ_{B} was reduced to 0.6 ± 0.2 eV. When changing the cathode from Al to Al:Li in a single layer reference device, there was no change in the EA spectrum save that of increasing the built in field by 0.5 V. In the analysis of the data, the effect of the interfacial field is subtracted away. This means that only the response of the bulk material to the applied field is used to work out the field distribution of the bilayer device, independently of differences in interfaces.

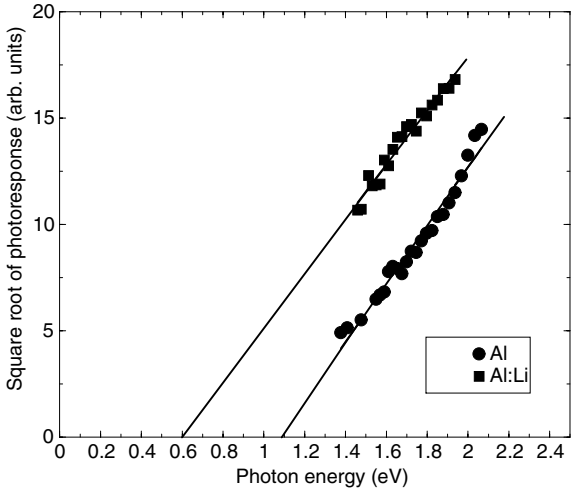

Fig. 2. The internal photoemission measurement of the Schottky energy barrier from Al and Al:Li cathodes to the Alq LUMO. The sample structures were ITO/Alq(130 nm)/Al and ITO/Alq(130 nm)/Al:Li. The sample with the Al cathode was held at a forward bias of 6 V, the sample with the Al:Li cathode was at a forward bias of +4 V.

2.3. Analysis of EA data

The analysis of EA data from multilayer devices has been carried out for several devices [4–6]. In this paper we have followed the procedure described by Rohlfing et al. [4] for analysing low molar mass devices. In order to extract the magnitude of the electric field in each layer of a multilayer device from EA data, reference EA spectra must be found for each individual layer under a known bias or electric field. The spectral features of each layer can then be identified. Fig. 3 shows a series of EA spectra taken at the fundamental frequency (Ω) as a function of photon energy of an (a) ITO/Alq/Al:Li and (b) ITO/NPB/Al:Li device measured with an ac voltage of 0.5 V and with various dc biases. The difference between any two EA spectra taken at the fundamental frequency measured at any dc bias will remove the contribution of E_{i}. This can be seen from Eq. (3),

$$2E_{\mathrm{ac}}(E_{\mathrm{i}} + E_{\mathrm{dc1}})\cos(\omega t) - 2E_{\mathrm{ac}}(E_{\mathrm{i}} + E_{\mathrm{dc2}})\cos(\omega t) = 2E_{\mathrm{ac}}(E_{\mathrm{dc1}} - E_{\mathrm{dc2}})\cos(\omega t).$$

This difference spectrum will give the same lineshape as the EA spectrum taken at the second harmonic frequency (2Ω), which only depends on the bulk. Fig. 4, where the first harmonic frequency is measured with an ac voltage of 0.5 V, and the second harmonic frequency with an ac voltage of 0.7 V, confirms this for our results. In the analysis of multilayer low molar mass devices, the effect of the interfacial field is removed, and as a convention, the first harmonic EA spectrum obtained with 0 V dc bias is subtracted from the first harmonic EA spectra taken at nonzero dc

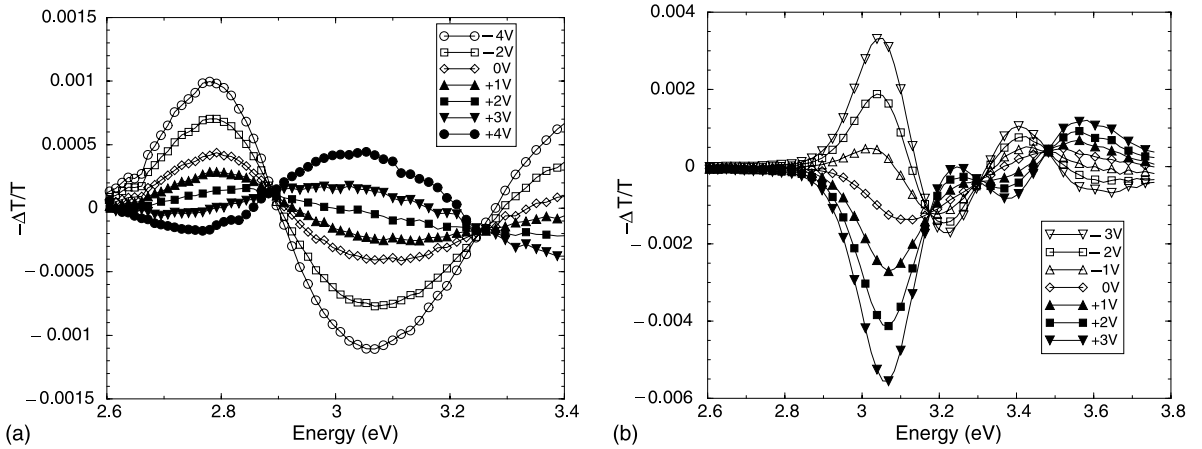

Fig. 3. The first harmonic EA spectrum of an Alq single layer device (ITO/Alq/Al:Li) (panel (a)) and an NPB single layer device (ITO/NPB/Al:Li) as a function of dc bias (panel (b)). $V_{ac} = 0.5$ V.

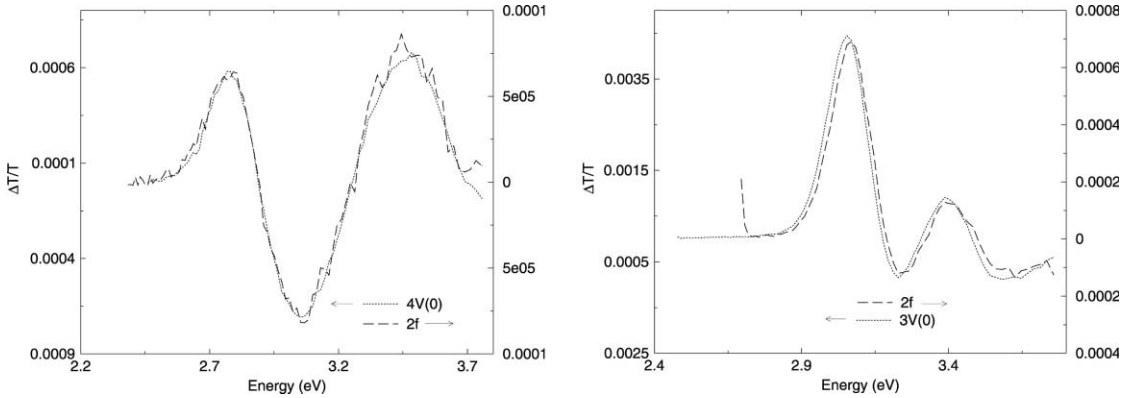

Fig. 4. Comparison of the second harmonic EA response measured with $V_{ac} = 0.7$ V with the difference between two first harmonic spectra for the ITO/Alq/Al:Li device (left-hand panel) and the ITO/NPB/Al:Li device (right-hand panel).

bias. This approach was also adopted by Rohlfing et al. [4].

Fig. 5 shows the first harmonic spectra at various biases from Fig. 3, with the first harmonic data at zero bias subtracted from each spectrum. At an energy of 2.78 eV, the EA response of Alq shows a peak whereas at this energy, NPB only shows a small response. Any peak at 2.78 eV in the EA response of the bilayer device can therefore be considered mainly from the Alq layer. At an energy of 3.05 eV, both Alq and NPB show a peak in the EA response. The NPB response is much stronger than the Alq response—about 8 times bigger. This has also been seen in EA studies on films of organic materials with coplanar electrodes [4]. In both Alq and NPB, the subtracted first harmonic EA peak in Fig. 5 scales linearly with the applied dc voltage; this property is essential for the analysis of the double layer devices.

Fig. 6 shows the first harmonic spectrum of a bilayer device of ITO/NPB/Alq/Al:Li device measured with an ac bias of 1 V. The first harmonic EA data at zero bias has been subtracted from the raw data. The data exhibits a small peak at 2.78 eV, mainly coming from the response of the Alq layer, and a larger peak at 3.05 eV, coming from

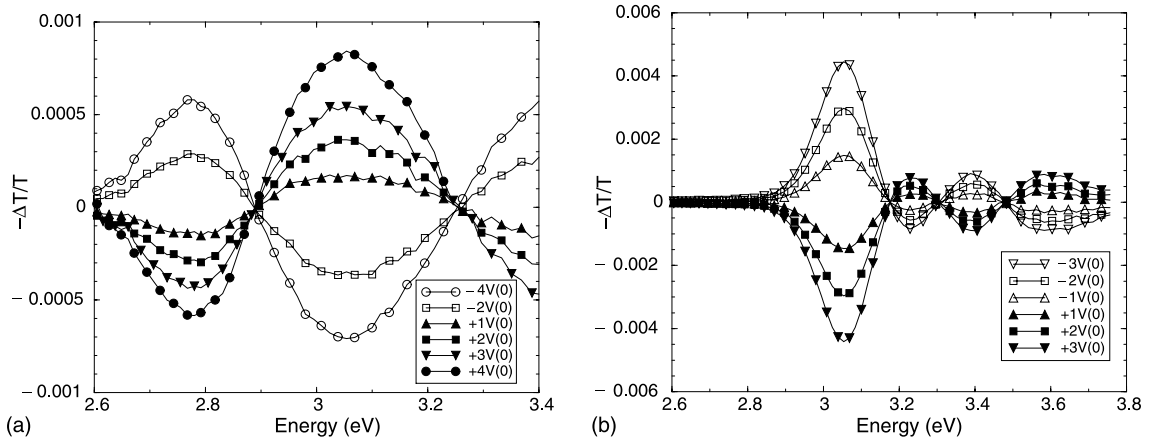

Fig. 5. First harmonic EA spectra of the Alq single layer device (panel (a)) and the NPB single layer device (panel (b)) at nonzero V_{dc} minus the EA spectrum at measured at 0 V dc bias.

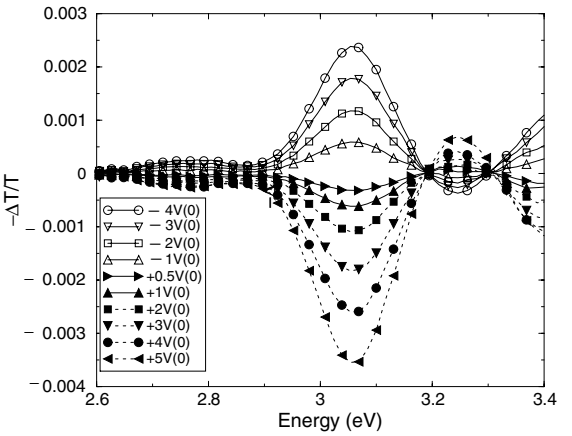

Fig. 6. First harmonic EA spectra of a double layer device of ITO/NPB/Alq/Al:Li at dc biases from −4 to +5 V with the EA spectrum at $V_{dc} = 0$ V subtracted. $V_{ac} = 1$ V.

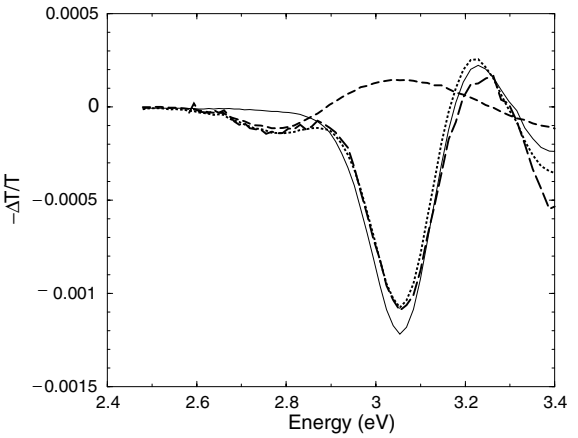

Fig. 7. First harmonic EA spectrum of the double layer device—see caption for the previous figure—at +2 V minus the spectrum at 0 V (long dashed line), compared with a linear combination of the single layer NPB and Alq response (dotted line), scaled to give the best fit linear combination to the bilayer device data. The short dashed line is the Alq response, the solid line the NPB response.

the response of both the Alq and NPB layer. By appropriately scaling the single layer NPB and Alq response (with the 0 V data subtracted) and taking a linear combination a fit could be obtained to the bilayer data at each bias. Fig. 7 illustrates this for a dc bias of +2 V. The average electric field across each organic layer in a bilayer device can therefore be found as a function of applied dc bias. These measured fields are presented in Section 4. A similar analysis was performed on the EA data obtained for the ITO/NPB/Alq/Al device.

3. Device simulation method

The devices were simulated using a one-dimensional time-independent drift–diffusion model, which involves finding a self-consistent solution for the following sets of equations with Schottky contact boundary conditions.

Firstly, the time-independent current continuity equations,

$$\frac{dJ_n}{dx} = -q(G - R), \tag{5}$$

$$\frac{dJ_p}{dx} = q(G - R), \tag{6}$$

where J_n and J_p are the electron and hole current densities respectively, G is the electron–hole pair generation rate (neglected), and q is the electron charge magnitude. R is the optical recombination rate and has a bimolecular form for exciton formation, with a Langevin recombination coefficient, γ,

$$R_{opt} = \gamma(np), \tag{7}$$

$$\gamma = \frac{4\pi q \mu_R}{\epsilon}, \tag{8}$$

where μ_R is an effective recombination mobility, taken to be the larger of the electron and hole mobilities in the material, and ϵ is the dielectric constant of the material [22].

Secondly, Poisson's equation relating the electrostatic potential, ψ, or the electric field, E, with the charge in the device,

$$\frac{dE}{dx} = -\frac{d^2\psi}{dx^2} = \frac{q}{\epsilon}(p - n - N_A^- + N_D^+), \tag{9}$$

where N_A^- and N_D^+ are the ionised acceptor and donor impurity concentrations. The equations relating electron and hole densities to the electrostatic potential are derived from the Maxwell–Boltzmann distribution,

$$n = N_C \exp\left[\frac{q}{k_B T}\left(\psi - \phi_n + \frac{\chi_c}{q}\right)\right], \tag{10}$$

$$p = N_V \exp\left[-\frac{q}{k_B T}\left(\psi - \phi_p + \frac{E_g}{q} + \frac{\chi_c}{q}\right)\right], \tag{11}$$

where ϕ_n and ϕ_p are the electron and hole quasi-Fermi levels, respectively, and χ_c is the electron affinity of the material.

The drift–diffusion equations defining the electron and hole currents, J_n and J_p,

$$J_n = -q\mu_n n\frac{d\phi_n}{dx}, \tag{12}$$

$$J_p = -q\mu_p p\frac{d\phi_p}{dx}. \tag{13}$$

J_n and J_p include both drift and diffusion components, and μ_n and μ_p are the electron and hole mobilities respectively. These mobilities have been shown to be field dependent (for example [23,24]) and take the form below at constant T,

$$\mu_n(E) = \mu_{n0}\exp\left(\sqrt{\frac{E}{E_0}}\right), \tag{14}$$

$$\mu_p(E) = \mu_{p0}\exp\left(\sqrt{\frac{E}{E_0}}\right), \tag{15}$$

where μ_{n0} and μ_{p0} are the zero field mobilities, and E_0 is a constant related to the disorder in the material.

3.1. Schottky contact boundary conditions

At the metal–organic (Schottky) contacts, there are three boundary conditions. Firstly, the electrostatic potential ψ_b can be determined from the work function of the metal, ϕ_m, and the electron affinity of the organic material, χ_c,

$$\psi_b = -\phi_{bn} = -(\phi_m - \chi_c), \tag{16}$$

where ψ_b is the electrostatic potential at the contact, and ϕ_{bn} is the barrier to electron injection from the contact into the bulk. The barrier to hole injection at the contacts, ϕ_{bp}, is given by

$$\psi_{bp} = E_g - \phi_{bn} = E_g - (\phi_m - \chi_c). \tag{17}$$

The electron and hole current densities at the contacts, J_{nb} and J_{pb}, consist of three components: thermionic emission, a backflowing interface recombination current (the time-reversed process of thermionic emission), and tunnelling [12]. These currents can be described in terms of an effective recombination velocity, v_{rn} and v_{rp} respectively,

$$J_{nb} = qv_{rn}(n_b - n_{eq}) + (J_{tn} - J_{tn0}), \tag{18}$$

$$J_{pb} = -qv_{rp}(p_b - p_{eq}) - (J_{tp} - J_{tp0}), \tag{19}$$

where n_{eq} and p_{eq} are the electron and hole densities at the contact at thermal equilibrium, n_b and p_b are the carrier densities at the contacts, and J_{tn} and J_{tp} are the Fowler–Nordheim tunnelling contributions to the Schottky boundary conditions. J_{tn0} and J_{tp0} are the values of J_{tn} and J_{tp} at zero bias. Charge injection and recombination at the metal–organic interface has been shown to give rise to the following expression for v_{rn}:

$$v_{rn} = 16\pi\epsilon\mu_n(k_B T)^2/q^3, \tag{20}$$

with a similar expression for v_{rp} in which μ_n is replaced by μ_p [25].

The Fowler–Nordheim currents take the form [26]

$$J = CE^2 \exp\left(\frac{-\kappa}{E}\right), \tag{21}$$

where κ varies with the barrier height,

$$\kappa = \frac{8\pi\sqrt{2em}}{3h}\phi_b^{3/2}, \tag{22}$$

$$C = \frac{3e^2}{8\pi h\phi_b}. \tag{23}$$

The model also incorporates image force lowering of the barrier at the contacts [27],

$$\phi_{eff} = \phi_b - \Delta\phi_b = \phi_b - \sqrt{\frac{qE}{4\pi\epsilon}}, \tag{24}$$

provided that the field at the contact has the correct sign for barrier lowering. The value of the dielectric constant, ϵ, is typically about 3.0, whereas in typical inorganic semiconductors ϵ is about 12 (Si) or 14 (GaAs). Consequently, it can be seen from the above expression for image force lowering that the effect is much more pronounced in organic semiconductors than in inorganic ones, owing to the lower dielectric constant.

3.2. Parameters

Table 1 contains the material parameters used in the simulation which were obtained from references. The mobilities of the minority carriers (μ_n in NPB and μ_p in Alq) have been assumed to be two orders of magnitude lower than that of the majority carriers, such that the materials act as preferential hole or electron transporters. The concentration of dopants is not well characterised and is highly sample dependent. The values shown in the table are low enough to not significantly affect the results.

Table 1
Material parameters used in the simulation

Parameter	NPB	Alq
ϵ_s	3.0 [18]	3.0 [18]
μ_{n0} ($m^2 V^{-1} s^{-1}$)	6.1×10^{-10} [18]	1.9×10^{-10} [18]
μ_{p0} ($m^2 V^{-1} s^{-1}$)	6.1×10^{-8} [18]	1.9×10^{-12} [18]
E_0 ($V m^{-1}$)	4.44×10^7 [18]	7.1×10^6 [18]
N_C (m^{-3})	1×10^{27} [18]	1×10^{27} [18]
N_V (m^{-3})	1×10^{27} [18]	1×10^{27} [18]
N_A^- (m^{-3})	1×10^{15}	
N_D^+ (m^{-3})	–	1×10^{15}
E_g (eV)	3.0 [9]	2.7 [9]
χ_c (eV)	2.4 [9]	3.0 [9]

Although the simulation naturally requires quite a large number of material parameters as input, only a few are critical in terms of obtaining the correct results in this context. As we will demonstrate in the next section, the important parameters are the barrier heights to carrier injection (ϕ_{bn} and ϕ_{bp}) and the offsets between the HOMO and LUMO levels of NPB and Alq. For example, even if the mobility of the majority carrier were to vary by as much as an order of magnitude, it would only affect the precise numeric values obtained from the simulation whilst the qualitative behaviour would remain largely unchanged.

We examined the possibility of traps in the Alq layer in our model, at an energy level of 0.15 eV and a density of 1.3×10^{23} m^{-3} from [28], using the method described in [11]. However, the inclusion of traps was found to make no discernible difference to the results obtained.

4. Results

Figs. 8, 10 and 11 show the simulated and experimentally measured average electric fields in each layer as a function of applied bias for IT0/NPB/Alq/Al, ITO/NPB/Alq/Al:Li and ITO/NPB/

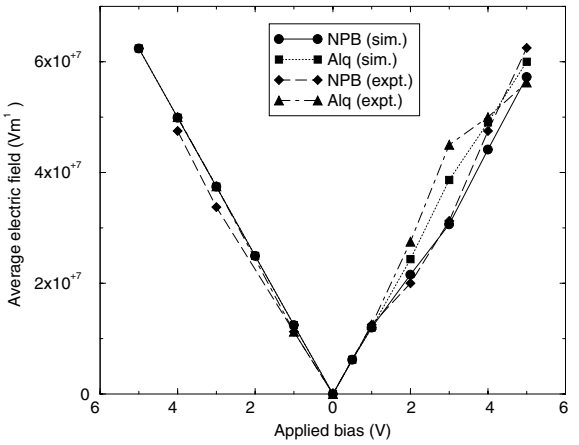

Fig. 8. Comparison of simulated and measured average fields in the ITO/NPB/Alq/Al device.

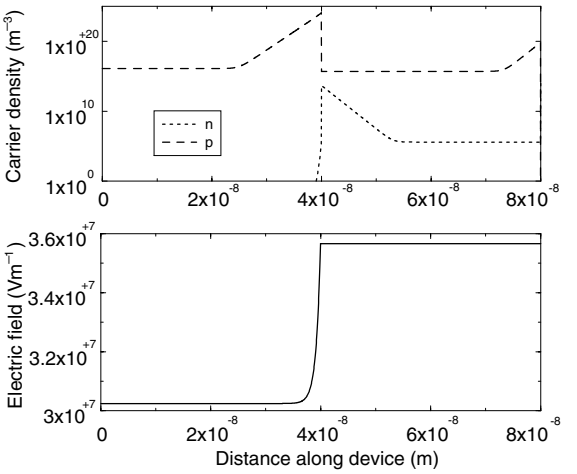

Fig. 9. Electric field profile (bottom panel) and carrier density profiles (top panel) through the ITO/NPB/Alq/Al device at +3 V. The ITO contact is at $x = 0$, where x is the distance along the device.

Alq/Mg:Ag devices, respectively. The built-in field has been subtracted from the simulated data to allow direct comparison with the data obtained by EA spectroscopy.

4.1. ITO/NPB/Alq/Al device

In Fig. 8, good agreement between the experimental and simulated data can be seen. The barrier to hole injection, ϕ_{bp}, at the ITO/NPB interface used in the simulation was 0.7 eV [9,29] and the barrier to electron injection, ϕ_{bn}, at the Alq/Al interface was taken as 1.2 eV (its measured value is 1.1 ± 0.2 eV—see Section 2). Although it is well known that the workfunction of ITO varies from 4.7 to 5.2 eV (e.g. [30]), the value of 4.7 eV was chosen as it provided a good fit to the experimental data. The effect of changing the workfunction of ITO is discussed below.

Under small forward bias conditions, the electric field is homogeneous across the device due to negligible charge injection from either contact since $V_{app} < V_{bi}$. As the applied bias is increased above V_{bi}, holes are injected into the NPB layer from the ITO contact; due to the large barrier height, electron injection into the Alq layer from the Al contact is negligible. The holes injected into the NPB layer build up at the NPB/Alq interface due to the offset between the HOMO bands, hence the Alq acts as a hole blocking layer. This charge build up causes the field to increase in the Alq layer in accordance with Poisson's equation. Fig. 9, which shows the electric field and carrier density profiles obtained from the device simulation ($V_{app} = +3$ V), demonstrates this point. Similar explanations have been offered by Hiramoto et al. [7] and Ruhstaller et al. [17]. The presence of hole accumulation at an interface has been deduced from transient current measurements on a TPD/Alq device by Matsumura et al. [31].

As the applied forward bias is increased further, the experimental curves can be seen to converge and cross, with the average electric field in the NPB layer being larger than that in the Alq layer. A possible explanation for this behaviour is that at higher fields, electrons are injected over the barrier from the Al cathode into the Alq layer, and accumulate at the heterojunction (on the Alq side), where the offset between the LUMO levels is 0.6 eV (see Fig. 1), i.e. the NPB acts as an electron blocking layer. This negative charge build up would reduce the magnitude of the field in the Alq layer. A convergence of the curves is observed in the simulated data, but they do not cross and the field in the Alq layer remains the greater. However, the model does show increasing electron

accumulation in the Alq layer at higher biases, which accounts for the convergence of the curves.

Varying the workfunction of ITO from 4.7 to 5.2 eV would result in a range of barrier heights to hole injection (ϕ_{bp}) ranging from 0.2 to 0.7 eV. Since the barrier to electron injection (ϕ_{bn}) is much larger (1.2 eV), the qualitative behaviour of the field distribution would be unchanged, with significant hole injection, negligible electron injection, and the accumulation of holes at the interface resulting in the average field in the Alq layer being larger than that in the NPB layer. If the barrier to hole injection at the ITO contact was decreased, the average field in the Alq layer would be even greater, as more holes would be injected into the system and hence accumulate at the interface. If the barrier was increased, hole injection and consequently accumulation at the interface would decrease; the magnitude of the average field in the Alq layer would be smaller than in the present situation, but it would still be the larger of the two average fields.

In reverse bias, the field across the device is homogeneous, with the average fields in each layer being equal (see Fig. 8), since virtually no charge is injected and the device is fully depleted. This explanation holds for all three devices. The simulated curves lie exactly on top of each other, along with the experimental Alq curve. The experimental NPB curve sits slightly below the experimental Alq curve, but they are the same within experimental error.

4.2. ITO/NPB/Alq/Al:Li device

Fig. 10 again shows good agreement between theory and experiment. In order to simulate this device, all parameters were unchanged except for the electron barrier, ϕ_{bn}, which was set as 0.6 eV as this gave the best fit to the experimental data and is consistent with the measured value reported in Section 2.

As for the device discussed in Section 4.1, there is little charge injection into the device at small biases and so the field is homogeneous across the two layers. For larger forward biases, there is significant electron injection from the Al:Li cathode into the Alq layer. The electron barrier at the Al/Al:Li interface is smaller than the hole barrier at the ITO/NPB interface. There is a large LUMO level offset at the NPB/Alq interface of 0.6 eV (see Fig. 1) so that the NPB acts as an electron blocking layer. These two factors result in a large electron density in the Alq layer and a build up of electrons at the heterojunction. There is a large hole density in the NPB layer including the hole build up at the heterojunction, and this distribution of charges results in the average field in the NPB layer being greater than that in the Alq layer, again in accordance with Poisson's equation.

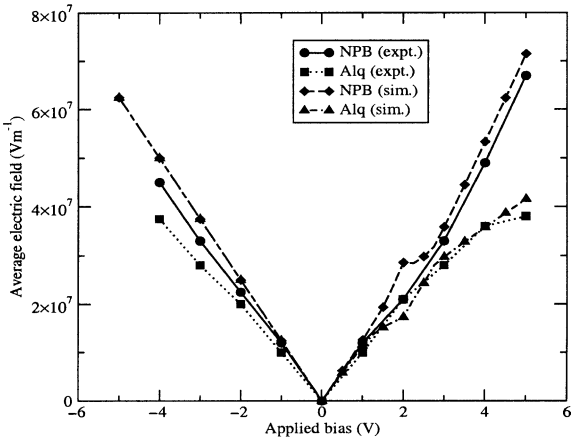

Fig. 10. Comparison of simulated and measured average fields in the ITO/NPB/Alq/Al:Li device.

In the simulation of this device, the values of the electrode workfunctions used are critical. Since the barrier height to electron injection ϕ_{bn} at the Alq/Al:Li interface is smaller than for the previous device, it now injects a significant number of electrons. These electrons accumulate at the organic–organic interface and can determine which layer has the greater average value of the electric field. If $\phi_{bp} < \phi_{bn}$, a larger number of holes than electrons will be injected, accumulate at the interface and cause a larger field to form in the Alq layer; the reverse situation occurs if $\phi_{bn} < \phi_{bp}$. If the barrier heights are equal, the field will be greater in the NPB layer as the band offset between the LUMO levels in the materials is greater than that for the HOMO levels, causing a greater confinement of electrons at the heterojunction, reducing the field in the Alq layer.

4.3. ITO/NPB/Alq/Mg:Ag device

Rohlfing et al. [4] used EA spectroscopy in experimental measurements of the average electric fields in each layer of an ITO/NPB/Alq/Mg:Ag device with layer thicknesses of 100 and 200 nm for the NPB and Alq layers respectively as a function of V_{app}. They also investigated the electric field distribution using EA spectroscopy for ITO/NPB/Alq/Mg:Ag devices with various thicknesses of Alq and NPB [15]. They found that the thicknesses of the layers made a quantitative difference to the average fields in each layer, but qualitatively the behaviour was found to be the same, indicating that the fields are primarily determined by the barriers to carrier injection and the accumulation of carriers at the interface.

The parameters used to simulate this device were unchanged except for the layer thicknesses and ϕ_{bn}. The value for the barrier to electron injection (ϕ_{bn}) at the Mg:Ag contact used in the simulation was set at 1.1 eV. Although this is larger than published values of 0.7 eV (e.g. [29]), this produced qualitatively the measured electric field distribution. Using a value of 0.7 eV for ϕ_{bn} in the device simulation produced an average electric field in the NPB layer greater than that in the Alq layer, due to significant electron injection and accumulation at the NPB/Alq interface.

Under forward bias conditions, it can be seen from Fig. 11 that there is good agreement between the experimental and simulated values of the average electric field in the Alq layer; both show that the average field in the NPB layer is smaller than in the Alq layer. As can be seen from the carrier density and field profiles at $V_{app} = +4$ V in Fig. 12, the electron density in the Alq layer is considerably smaller than the hole density in this layer. Combined with the accumulation of holes in the NPB layer at the interface, this accounts for the field in the Alq exceeding that in the NPB layer. The good agreement between theory and experiment for the Alq layer indicates that the hole charge accumulation at the NPB/Alq interface is predicted accurately in the device simulation.

However, the agreement between the experimental and simulated average electric field values in the NPB layer is disappointing. Although they

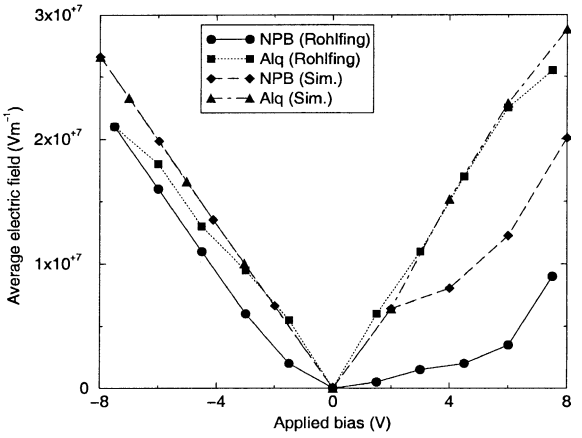

Fig. 11. Comparison of simulated and measured average fields in the ITO/NPB/Alq/Mg:Ag device.

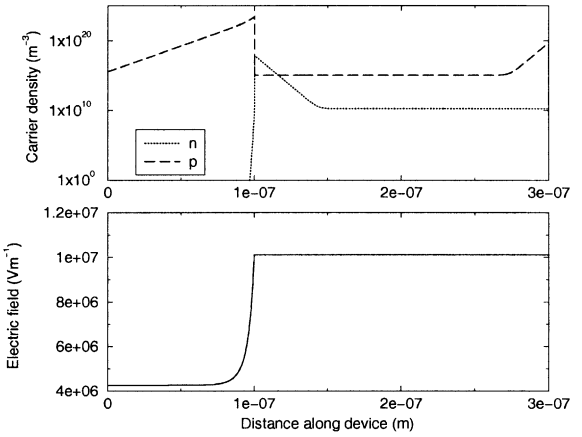

Fig. 12. Electric field profile and carrier density profiles through the ITO/NPB/Alq/Mg:Ag device at +4 V.

both exhibit similarly shaped curves, the magnitudes of the curves vary considerably. Our simulated NPB curve follows the simulated and experimental Alq curves under small forward bias conditions ($V_{app} < 2$ V), as we expect due to negligible charge injection. As the applied bias increases, the number of holes injected into the NPB layer increases, whilst few electrons are injected into the Alq layer, resulting in a larger average electric field value in the Alq layer for the reasons outlined above. The experimental data of Rohlfing et al. [4] shows that even under small forward bias (including $V_{app} < V_{bi}$), the average field in the layer

NPB is smaller than that in the Alq layer. In fact, the field in the NPB layer is shown by Rohlfing et al. [8] to be smaller for $V_{app} < V_{bi}$ in forward bias than under the corresponding reverse bias. We expect the field in each layer to be equal for all reverse biases and forward biases below V_{bi} due to the negligible injection of charge. This situation is observed in our simulation of this device, and in Sections 4.1 and 4.2. At an applied bias of +4 V, the average field in the Alq is a factor of about 10 times greater than in the NPB according to Rohlfing et al. [8], whereas we obtained a factor of about 2. From Fig. 9(a) of Ruhstaller et al. [17], this factor is about 3. The large factor seen in Rohlfing et al. [8] cannot be explained in terms of charge injection and accumulation, since under conditions of small forward bias (i.e. $V_{app} < V_{bi}$), charge injection is negligible.

Again, under reverse bias, we obtain a homogeneous electric field distribution across the device from our simulation, for reasons previously outlined. Rohlfing et al. [4] state that under reverse bias, the average field in both layers is identical within the accuracy of the experiment and the distribution is due to negligible charge injection. In this case, the agreement between our simulated average field values and their measured average field values is good (see Fig. 12).

5. Conclusions

The combination of EA spectroscopy and our drift–diffusion device simulation has been shown to be an aid to understanding charge injection and distribution in bilayer OLEDs. In particular, we have demonstrated the use of an interface between two layers that preferentially transport one type of carrier to the other to confine carriers which is vital for effective optical recombination. Furthermore, when coupled with EA data, our device model can produce some useful information. For example, in the case of the device studied by Rohlfing et al. [4], the value of ϕ_{bn} at the Mg:Ag electrode calculated from the metal workfunction (ϕ_m) is incorrect. Such parameters are essential in the accurate simulation of OLEDs e.g. J–V characteristics.

This work also shows that the barrier heights to carrier injection and the offset between the HOMO and LUMO levels at the heterointerface (i.e. the presence of blocking layers) critically affect charge accumulation, and hence the electric field distribution in the device. This also has wider implications in terms of current transport and device efficiency.

The agreement between the simulated average field values and those obtained experimentally by EA spectroscopy is good, especially for the ITO/NPB/Alq/Al (Fig. 8) and ITO/NPB/Alq/Al:Li device (Fig. 11) devices. In addition, the average electric fields simulated for the ITO/NPB/Alq/Mg:Ag (Fig. 12) were in quite good agreement with the published data [4]. The data in reverse bias showed good agreement, as did the average fields in the Alq layer in forward bias. However, the very low fields measured in the NPB layer under forward bias by Rohlfing et al. [4] need further consideration.

Acknowledgements

SJM and MAW acknowledge studentships from the Engineering and Physical Sciences Research Council and SJM would like to thank Sharp Laboratories of Europe for additional funding.

References

[1] C.W. Tang, S.A. VanSlyke, Appl. Phys. Lett. 51 (1987) 913.
[2] C.W. Tang, S.A. VanSlyke, C.H. Chen, J. Appl. Phys. 65 (1989) 3610.
[3] J.H. Burroughes, D.D.C. Bradley, A.R. Brown, R.N. Marks, K. Mackay, R.H. Friend, P.L. Burns, A.B. Holmes, Nature 47 (1990) 539–541.
[4] F. Rohlfing, T. Yamada, T. Tsutsui, J. Appl. Phys. 86 (1999) 4978.
[5] I.H. Campbell, M.D. Joswick, I.D. Parker, Appl. Phys. Lett. 67 (1995) 3171.
[6] P.A. Lane, J. Rostalski, C. Giebeler, S.J. Martin, D.D.C. Bradley, D. Meissner, Solar Energy Mater. Solar Cells 63 (2000) 3.
[7] M. Hiramoto, K. Koyama, K. Nakayama, M. Yokoyama, Appl. Phys. Lett. 76 (10) (2000) 1336.

[8] F. Rohlfing, D.D.C. Bradley, Chem. Phys. 227 (1998) 133.
[9] S. Berleb, W. Brütting, G. Paasch, Organic Electronics 1 (2000) 41.
[10] L. Bozano, S. Carter, J.C. Scott, G.G. Malliaras, P.J. Brock, Appl. Phys. Lett. 74 (8) (1999) 1132–1134.
[11] C.D.J. Blades, A.B. Walker, Synth. Met. 111–112 (2000) 335.
[12] P.S. Davids, I.H. Campbell, D.L. Smith, J. Appl. Phys. 82 (1997) 6319.
[13] G.G. Malliaras, J.C. Scott, J. Appl. Phys. 83 (1998) 5399.
[14] J.C. Scott, S. Karg, S.A. Carter, J. Appl. Phys. 82 (1997) 1454.
[15] T. Yamada, F. Rohlfing, T. Tsutsui, Jpn. J. Appl. Phys. 39 (2000) 1382–2386.
[16] B.K. Crone, P.S. Davids, I.H. Campbell, D.L. Smith, J. Appl. Phys. 87 (4) (2000) 1974.
[17] B. Ruhstaller, S.A. Carter, S. Barth, H. Riel, W. Riess, J.C. Scott, J. Appl. Phys. 89 (8) (2001) 4575.
[18] J. Staudigel, M. Stößel, F. Steuber, J. Simmerer, J. Appl. Phys. 86 (1999) 3895.
[19] R. Murayama, S. Kawami, T. Wakimoto, H. Sato, H. Nakada, T. Namiki, K. Imai, M. Nomura, in: Extended Abstracts of the 54th Autumn Meeting of the Japanese Society of Applied Physics, No. 3, 1993, p. 1127.
[20] P. Siguard, J.-N. Chazalviel, F. Ozanam, O. Stephan, J. Appl. Phys. 89 (2001) 466.
[21] R.H. Fowler, Phys. Rev. 38 (1931) 45.
[22] M. Pope, C.E. Swenburg, Electronic Processes in Organic Crystals, Oxford University Press, Oxford, 1982.
[23] P.W.M. Blom, M.J.M. de Jong, M.G. van Munster, Phys. Rev. B 55 (1997) 55.
[24] D.H. Dunlap, P.E. Parris, V.M. Kenkre, Phys. Rev. Lett. 77 (1996) 542.
[25] J.C Scott, G.G. Mallaras, Chem. Phys. Lett. 299 (1999) 115.
[26] R.H. Fowler, L. Nordheim, Proc. R. Soc. London 119 (1928) 173.
[27] M.S. Tyagi, Introduction to Semiconductor Materials and Devices, J Wiley & Sons, New York, 1991.
[28] W. Brütting, S. Berleb, A.G. Mückl, Organic Electronics 2 (2000) 1–36.
[29] M.A. Baldo, D.F. O'Brien, M.E. Thompson, S.R. Forrest, Phys. Rev. B 60 (1999) 14422.
[30] C. Giebeler, H. Antoniadis, D.D.C. Bradley, Y. Shirota, Appl. Phys. Lett. 72 (1998) 2448.
[31] M. Matsumura, A. Ito, Y. Miyamae, Appl. Phys. Lett. 75 (1999) 1042.